Journal of Materials Chemistry C

ROYAL SOCIETY OF CHEMISTRY

PAPER

View Article Online
View Journal | View Issue

Check for updates

Cite this: J. Mater. Chem. C, 2026, 14, 4775

Polymorphism-controlled charge transport in T-shaped π-conjugated crystals: high mobility *via* a double-column pathway

Suo Jeon,[a] Seiya Yokokura, *[ab] Pingyu Jiang,[c] Mingoo Jin,[c] Hiroki Waizumi[ab] and Toshihiro Shimada *[ab]

Organic semiconductors offer a unique platform for developing flexible, lightweight, and low-cost electronic materials, where charge-transport properties are highly sensitive to molecular packing and polymorphism. Understanding how molecular geometry and orbital alignment govern intermolecular electronic coupling is essential for achieving high mobility and structural robustness. Here, we report the design of a novel T-shaped π-conjugated molecule engineered to promote cooperative electronic couplings between adjacent π-stacking columns in the solid state. Temperature-controlled physical vapor transport (PVT) yielded two distinct polymorphs: a low-temperature (LT) form with a θ-type packing motif and a high-temperature (HT) form adopting a pitched π-stacking arrangement analogous to rubrene. Despite its lower density, the HT form exhibits shorter π–π distances and abundant C–H···π interactions that promote favorable orbital phase alignment and strong electronic coupling between two parallel stacking columns. This pathway, termed "double-column transport," constitutes a cooperative one-dimensional transport framework that enhances robustness against defects. Transfer-integral calculations predicted hole mobilities an order of magnitude higher for the HT form, and single-crystal transistor measurements confirmed this trend, yielding a maximum mobility of 1.2 $cm^2 V^{-1} s^{-1}$. These findings demonstrate that charge-transport performance in polymorphic organic semiconductors is governed not by packing density but by orbital phase matching, establishing polymorph control and double-column transport design as effective strategies for realizing robust, high-mobility organic semiconductors.

Received 12th November 2025,
Accepted 27th January 2026

DOI: 10.1039/d5tc04018c

rsc.li/materials-c

Open Access Article. Published on 28 January 2026. Downloaded on 5/23/2026 3:30:11 PM.
This article is licensed under a Creative Commons Attribution-NonCommercial 3.0 Unported Licence.

Introduction

Organic semiconductors have attracted considerable attention for applications in flexible, lightweight, and low-cost electronics, including transistors, sensors, and photovoltaic devices.[1–3] Their charge-transport properties are highly sensitive to molecular packing motifs in the solid state, and even subtle changes in crystal structure can lead to dramatic differences in device performance.[4–6] A well-known example is the contrast between tetracene and rubrene: tetracene crystallizes in a herringbone packing arrangement with moderate hole mobility, whereas rubrene, bearing four phenyl substituents, adopts a pitched π-stacking structure that affords large transfer integrals and significantly higher mobility.[7–10] These studies underscore the importance of crystal engineering and polymorphism in tailoring the functionality of organic semiconductors.[11–13]

In recent years, considerable efforts have been devoted to enhancing charge mobility through polymorph control and molecular design.[14–16] Crystal polymorphism has been shown to play a decisive role in charge transport, where distinct packing motifs of the same molecule can result in markedly different mobilities.[17,18] Strategies such as tuning sublimation conditions to selectively obtain high-mobility phases,[19–21] introducing substituents to alter stacking motifs,[22–24] and designing extended π-conjugated frameworks have all been reported.[25–28] These approaches highlight the potential of molecular packing engineering to boost device performance, yet in most cases the resulting charge transport remains essentially one-dimensional,[29] and the impact of cooperative interactions between multiple stacking columns has rarely been explored.

Traditionally, high carrier mobility has been correlated with dense molecular packing and an increased number of

[a] Graduate School of Chemical Sciences and Engineering, Hokkaido University, Kita 13 Nishi 8, Kita-ku, Sapporo, 060-8628, Japan. E-mail: seiyayokokura@eng.hokudai.ac.jp
[b] Division of Applied Chemistry, Faculty of Engineering, Hokkaido University, Kita 13 Nishi 8, Kita-ku, Sapporo, 060-8628, Japan
[c] Institute for Chemical Reaction Design and Discovery (WPI-ICReDD), Hokkaido University, Sapporo, Hokkaido 060-8628, Japan

Open Access Article. Published on 28 January 2026. Downloaded on 5/23/2026 3:30:11 PM. This article is licensed under a Creative Commons Attribution-NonCommercial 3.0 Unported Licence.

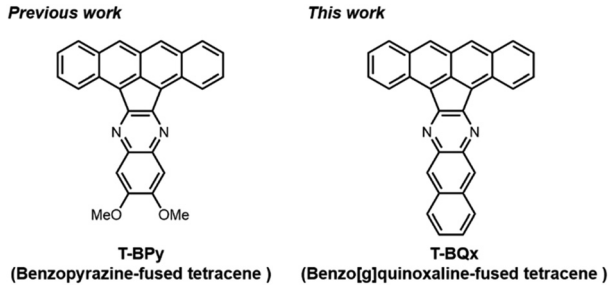

Fig. 1 Molecular structure of **T-BPy** and **T-BQx**.

intermolecular contacts.[30–32] However, recent insights suggest that the decisive factor is not packing density itself but the quality of orbital overlap, particularly orbital phase matching.[29,33–35] While this concept is beginning to reshape our understanding of charge transport in organic materials, direct experimental demonstrations linking polymorphism, orbital alignment, and transport efficiency remain scarce.

In this context, here we report the design of a novel T-shaped π-conjugated molecule, **T-BQx** (Benzo[*g*]quinoxaline-fused tetracene, Fig. 1), whose extended conjugation was intended to promote enhanced orbital overlap and cooperative electronic couplings between adjacent π-stacking columns in the crystal. Previously reported analogues, such as **T-BPy** (benzopyrazine-fused tetracene, Fig. 1) with substituents typically adopt one-dimensional stacking arrangements, described in the literature as ''herringbone-like one-dimensional columnar stacking,'' which limit their transport dimensionality.[36] In contrast, our system was designed to broaden the conjugated framework and explore new packing architectures. By temperature-controlled physical vapor transport (PVT), two distinct polymorphs were obtained: a low-temperature (LT) form with a θ-type packing motif and a high-temperature (HT) form adopting a pitched π-stacking arrangement reminiscent of rubrene. Remarkably, the HT form combines looser packing with favorable orbital alignment, leading to strong couplings between parallel stacking columns. We define this cooperative transport pathway as ''double-column transport,'' in which two parallel π-stacking columns are electronically coupled to form a modified one-dimensional transport topology with enhanced robustness against defects.

Experimentals

Synthetic procedures

A mixture of cyclopenta[*fg*]tetracene-1,2-dione (50 mg, 0.177 mmol) and 2,3-diaminonaphthalene (42 mg, 0.265 mmol) in AcOH (15 mL) and EtOH (20 mL) was heated overnight under reflux and nitrogen atmosphere. After cooling the reaction mixture, the precipitate was collected by suction filtration, washed with ethanol, and obtained as a crude product. The crude product was purified by vacuum sublimation to afford 60 mg of the desired compound in 90% yield. Due to its poor solubility, NMR spectra could not be recorded. Single crystals were subsequently grown from the purified sample by the physical vapor transport (PVT) method, the details of which will be described later.

Single-crystal X-ray analysis

Single-crystal X-ray structural analyses were carried out with a Rigaku XtaLAB PRO MM007 diffractometer using graphite-monochromated Cu Kα radiation at 153 K. The structures were solved with the SHELXT structure solution program using Intrinsic Phasing incorporated in the OLEX2 program package[37] and refined with the SHELXL package.[38] The hydrogen atoms were refined using the riding model. The crystal structures and packing motifs were analyzed for visualization by electronic and structural analysis program, Mercury 4.0.[39]

Theoretical calculation

The theoretical calculations were performed with the Gaussian 16W software package.[40] For the calculation of the transfer integrals (t), the molecular geometries extracted from the experimental crystal structure data were used without elaxation, and the calculation conditions were set to B3LYP/6-31G(d,p). For the reorganization energy (λ) calculation, B3LYP/6-31G(d,p)//B3LYP/6-31G(d,p) was used. With t and λ, the theoretical mobilities based on the hopping model were calculated in accordance with the literature.[41]

Single-crystal field-effect transistors

For measurements of the platelet-shaped crystals of the LT form, a bottom-gate bottom-contact configuration was employed using heavily doped n-type Si wafers with 500 nm SiO_2 layers as substrates. The substrates were cleaned by sonication in EtOH for 30 min, followed by ultraviolet–ozone treatment for 15 min, and subsequently treated with trimethoxy(1*H*,1*H*,2*H*,2*H*-heptadecafluorodecyl)silane (TCI Chemicals). Au source and drain electrodes (50 nm) were deposited directly onto the substrates by physical vapor deposition under $<5 \times 10^{-3}$ Pa. The Au electrodes were then modified with pentafluorobenzenethiol[42] (TCI Chemicals) by immersion in a 50 mM ethanol solution overnight under ambient conditions. The **T-BQx** platelet-shaped crystals were carefully transferred from the glass tube onto the SAM-treated substrates.

For measurements of the rod-shaped crystals of the HT form, top-gate top-contact transistors were fabricated using Parylene (diX-SR) as the gate dielectric. Carbon paste was applied onto the single-crystal surface to form the source and drain electrodes, and lead wires were attached. The two carbon electrodes were aligned so that current flowed along the π-stacking direction. A 700 nm-thick Parylene layer was deposited as the gate dielectric (C_i = 3.28 nF cm^{-2}), followed by deposition of Au gate electrodes on top of the insulator layer. The field-effect mobility (μ) was extracted from the saturation regime.

 This journal is © The Royal Society of Chemistry 2026

Open Access Article. Published on 28 January 2026. Downloaded on 5/23/2026 3:30:11 PM.
This article is licensed under a Creative Commons Attribution-NonCommercial 3.0 Unported Licence.

Results and discussions

Crystal growth and polymorphism

Two distinct polymorphs, platelet- and rod-shaped single crystals, were obtained by the physical vapor transport (PVT) method. A schematic diagram of the PVT setup is shown in Fig. 2. The raw material was placed in zone 1 and heated at 350 °C, yielding rod-shaped crystals at zone 2 (320 °C, HT form) and platelet-shaped crystals at zone 3 (240 °C, LT form). Powder XRD patterns of both forms matched well with the simulated patterns from single-crystal XRD analyses, confirming the high selectivity of polymorph growth under these conditions (Fig. S1). Under milder PVT conditions (zone 1 at 270 °C and zone 2 at 220 °C), only the LT form was obtained.

Crystal structure of the LT form

The LT form crystallizes in the $C2/c$ space group with $Z = 8$, containing one crystallographically independent molecule in the unit cell (Fig. 3 and Table S1). A π-stacking column is formed along the b-axis with an interplane distance of 3.494 Å. Although the molecule is polar, the stacking direction does not involve polarity inversion, resulting in a uniform π-stacking column. Inversion symmetry is present between neighboring stacking columns, cancelling the macroscopic polarization. The dihedral angle between neighboring molecules is 134.6°. This packing can be classified as a θ-type structure, in which one-dimensional charge transport is expected along the stacking column. The LT form exhibits an almost cofacial π–stacking arrangement with only slight displacement between adjacent molecules (Fig. 3(c)).

Crystal structure of the HT form

The HT form crystallizes in the *Pnma* space group with $Z = 4$ (Fig. 4 and Table S1). The molecular mirror plane coincides with a crystallographic mirror plane, and molecules are arranged in a pitched π-stacking motif with a large longitudinal displacement. This packing resembles the well-known high-mobility structure of rubrene. Similar to the LT form, polarity is not reversed within the π-stack, giving rise to uniform columns. The interplanar distance is 3.347 Å, shorter than in the LT form. Along the end-to-face (c-axis) direction, the polarization alternates between neighboring columns, giving rise to two distinct overlapping motifs: tetracene–tetracene and BQx–BQx contacts. The intermolecular dihedral angle in this direction is 62.6°, comparable to that reported for rubrene. Such a pitched π-stacking arrangement suggests the emergence of double-column transport pathways, where two parallel π-stacking

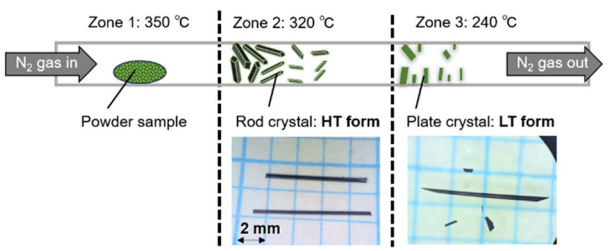

Fig. 2 Schematic illustration of the temperature-controlled PVT apparatus and photographs of two obtained polymorphs, HT and LT form.

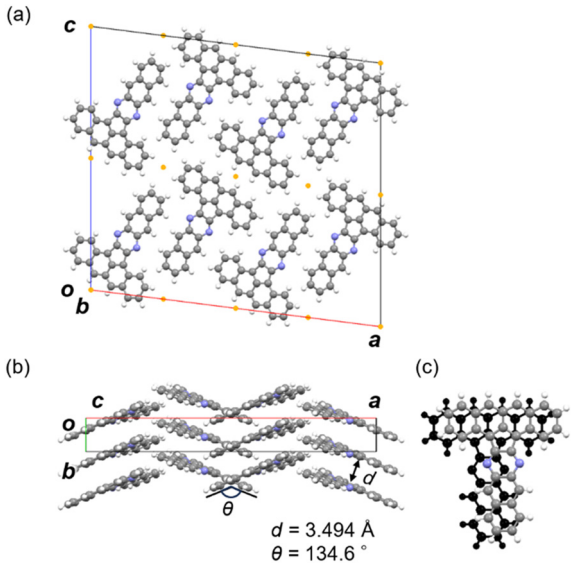

Fig. 3 (a) Crystal packing of the LT form viewed along the b-axis. The yellow dots indicate inversion centers. (b) Projection of the molecular stacking viewed along the c-axis, where d and θ represent the interplanar distance and the dihedral angle, respectively. (c) Face-to-face overlapping motif.

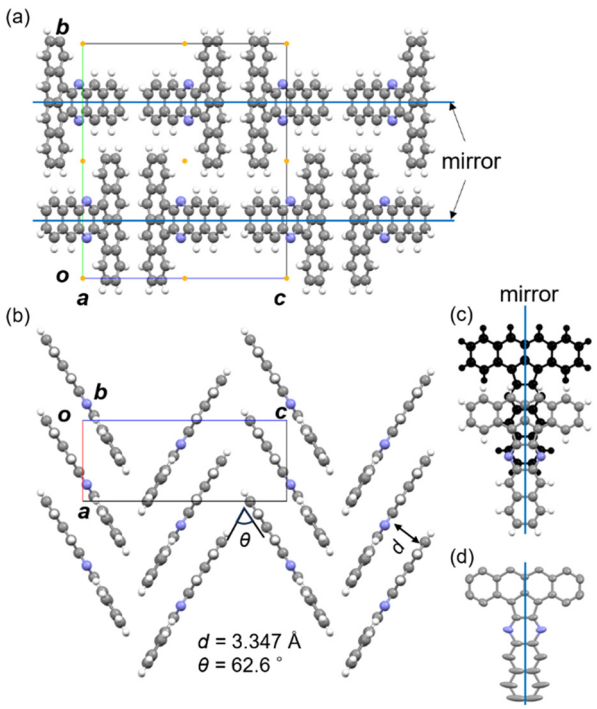

Fig. 4 (a) Crystal packing of the HT form viewed along the c-axis. The yellow dots indicate inversion centers. (b) Projection of the molecular stacking viewed along the a-axis, where d and θ represent the interplanar distance and the dihedral angle, respectively. (c) Face-to-face overlapping motif. (d) Molecular structure with thermal ellipsoids. Thermal ellipsoids are drawn at the 50% probability level. The blue lines indicate crystallographic mirror planes.

Open Access Article. Published on 28 January 2026. Downloaded on 5/23/2026 3:30:11 PM. This article is licensed under a Creative Commons Attribution-NonCommercial 3.0 Unported Licence.

columns cooperate to carry charge, providing greater defect tolerance than conventional single-column transport.

Anisotropic atomic displacement parameters were observed in the HT form (Fig. 4(d)). Elongated thermal ellipsoids were found along the molecular plane, particularly around the BQx site, suggesting dynamic deformation in the crystal. The crystal densities of the LT and HT forms were estimated to be 1.453 and 1.370 g cm^{-3}, respectively, indicating that the HT form packs more sparsely. This looser packing likely accounts for the enhanced flexibility. Remarkably, despite the lower density and greater dynamic disorder, the HT phase maintains a shorter face-to-face π–π distance, reinforcing its strong intermolecular electronic coupling.

Hirshfeld surface analysis

Hirshfeld surface analyses and fingerprint plots (Fig. 5 and Fig. S2) revealed distinct differences between the two polymorphs.

The Hirshfeld surface and fingerprint plots were calculated with CrystalExplorer21.5.[43]

In the LT form, H···H contacts are the most dominant, followed by C···C interactions, consistent with its overall denser molecular packing. However, despite the large number of close contacts, the orbital alignment within the θ-type motif is less favorable, resulting in limited electronic coupling and effectively one-dimensional charge transport.

In contrast, the HT form exhibits a much higher proportion of H···C contacts, reflecting the prevalence of C–H···π interactions within the pitched π-stacking motif. These interactions stabilize the tilted packing arrangement and, more importantly, are expected to facilitate favorable orbital overlap. Although the overall fraction of C···C contacts is smaller than in the LT form, the shorter π–π distance (3.347 Å) indicates potentially stronger electronic coupling along specific directions.

Taken together, these results suggest that charge-transport efficiency is not governed by the number of intermolecular contacts or packing density, but rather by the quality of orbital overlap and phase alignment. This interpretation is further supported by the transfer integral calculations presented in the following section, which quantitatively reveal the difference in electronic coupling between the LT and HT forms.

Molecular orbitals and energetics

The HOMO of **T-BQx** is delocalized across the entire T-shaped framework, whereas the LUMO is mainly localized on the tetracene moiety (Fig. 6(a)). HOMO and LUMO levels were −5.3 and −2.9 eV, respectively, suggesting that hole injection is more favorable. Diffuse reflectance spectra of polycrystalline samples gave an optical bandgap of 1.71 eV (see Fig. S3), smaller than the calculated HOMO–LUMO gap (2.4 eV), reflecting stabilization by intermolecular interactions. Reorganization energies were λ_h = 71.8 meV and λ_e = 221.0 meV. The small λ_h compared with rubrene (159 meV) and pentacene (95 meV) indicates that **T-BQx** is intrinsically favorable for hole transport.[44]

Transfer integral and theoretical mobility calculations

The theoretical charge-carrier mobilities were estimated using a hopping transport model based on the Marcus formalism, in which the mobility is determined by the intermolecular transfer integrals and the reorganization energy. This approach assumes incoherent charge transport *via* thermally activated hopping between neighboring molecules. This model was

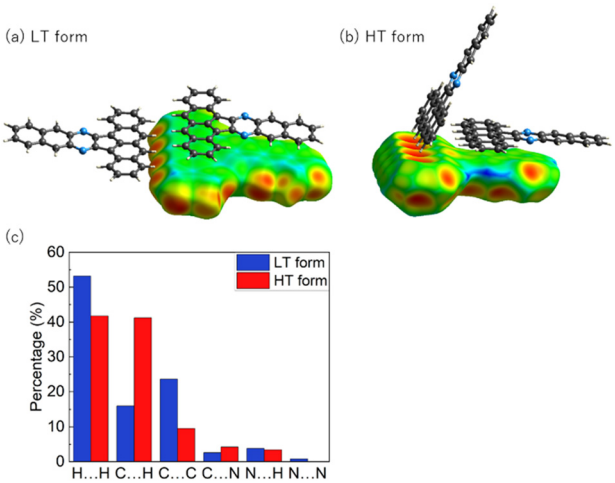

Fig. 5 Hirshfeld surface mapped with d_e (distance from the Hirshfeld surface to the nearest nucleus outside of the surface) of the **T-BQx** molecule in the crystal structure of (a) LT form and (b) HT form. (c) Intermolecular interactions on the Hirshfeld surface deconvoluted into ones between various atom types in LT (blue) and HT (red) form (%).

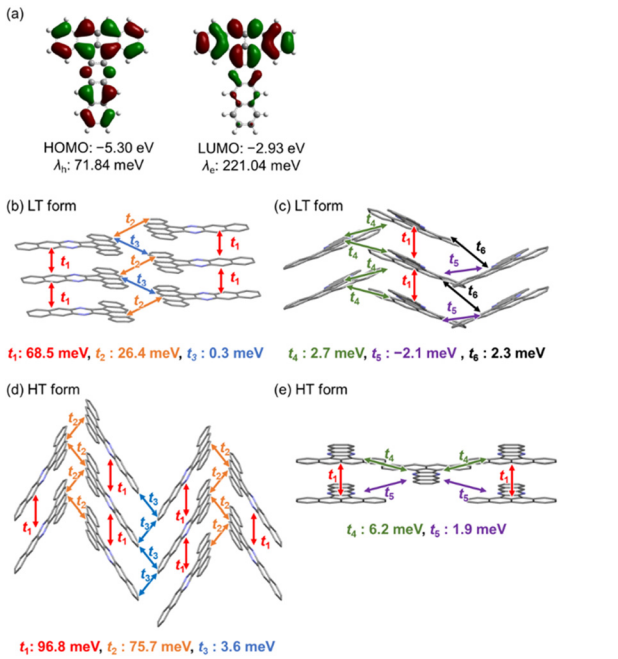

Fig. 6 (a) HOMO and LUMO of **T-BQx** molecule. Packing structures of the LT form viewed along (b) the molecular short axis and (c) the molecular long axis. The indicated values represent the intermolecular HOMO–HOMO transfer integrals. (d and e) Corresponding packing structures of the HT form viewed along the same directions.

 This journal is © The Royal Society of Chemistry 2026

Open Access Article. Published on 28 January 2026. Downloaded on 5/23/2026 3:30:11 PM. This article is licensed under a Creative Commons Attribution-NonCommercial 3.0 Unported Licence.

chosen because the temperature-dependent transistor measurements show thermally activated behavior, indicating that charge transport in the present system is dominated by hopping rather than band-like transport.

LT form. Transfer integrals for six dimers (t_1–t_6, Fig. 6(b) and (c)) were evaluated. The intra-column interaction along the stacking direction (t_1) is relatively large (68.5 meV), while all inter-column couplings, except for t_2, are negligibly small. This reflects both the intrinsically one-dimensional nature of the θ-type packing motif and the unfavorable phase alignment of molecular orbitals between adjacent columns. Notably, although the relative molecular positions of the t_2 and t_3 dimers are similar, their transfer integrals differ significantly due to orbital phase alignment: t_2 shows a moderate value, whereas t_3 is nearly zero. As a result, carrier transport between paired stacking columns becomes effectively one-way, further restricting charge transport in the LT form to a single π-stacking column. Based on t_1, the one-dimensional hole mobility was estimated to be $\sim$1 $cm^2\ V^{-1}\ s^{-1}$.

HT form. Five types of dimers (t_1–t_5, Fig. 6(d) and (e)) were identified in the HT form. The face-to-face overlap within the π-stacking column (t_1) afforded a very large transfer integral of $\sim$96.8 meV. Along the end-to-face direction, the tetracene–tetracene overlap (t_2) produced an exceptionally high value of 75.7 meV, which is larger than that reported for herringbone-packed tetracene crystals (70 meV).[45] This strong coupling originates from the mirror-plane symmetry of the pitched π-stacking motif, which enables excellent orbital phase matching. In contrast, the BQx–BQx overlap (t_3) yielded only a small transfer integral (3.6 meV), reflecting the limited π-conjugation of the BQx unit.

Taken together, the HT structure can be described as a cooperative one-dimensional "double-column" transport network, where two strongly coupled columns (t_1 and t_2) dominate charge transport, while couplings to neighboring columns through t_3–t_5 remain weak. Although the overall transport dimensionality remains one-dimensional, this configuration allows carriers to hop back and forth between the column pair, providing a transport pathway that is more tolerant to local defects compared with conventional single-column systems. The calculated one-dimensional hole mobility based on t_1 reached $\sim$15 $cm^2\ V^{-1}\ s^{-1}$, which is approximately one order of magnitude higher than that of the LT form. It should be emphasized that this double-column transport is fundamentally different from previously reported two-dimensional charge-transport networks, in which charge carriers delocalize over extended arrays of comparable intermolecular couplings in multiple directions. In the present system, strong electronic coupling is confined to a pair of parallel columns, while couplings in other directions remain weak, resulting in a cooperative but still one-dimensional transport topology rather than a true two-dimensional network.[46]

The transfer integrals between LUMOs were also calculated (see Table S2). In the LT form, the intra-column interaction (t_1) was relatively large (−67.6 meV); however, because the reorganization energy for electron transport is much higher than that for hole transport, the estimated electron mobility was only 0.40 $cm^2\ V^{-1}\ s^{-1}$. In the HT form, the transfer integral along the t_1 direction was even smaller, which can be attributed to the fact that the LUMO is mainly localized on the tetracene moiety, and the longitudinally displaced stacking in the HT form reduces the effective orbital overlap. Consequently, the electron mobility was estimated to be 1.9×10^{-3} $cm^2\ V^{-1}\ s^{-1}$.

Device characteristics

Because of the distinct crystal morphologies of the two polymorphs, identical device structures could not be fabricated. The platelet-shaped LT crystals and rod-shaped HT crystals require different transistor geometries to ensure reliable electrical contact and device operation. Therefore, tailored single-crystal FETs were prepared for each polymorph (Fig. 7(a) and Fig. S6). We note that differences in device architecture, including contact configuration and gate dielectric interfaces, can influence the absolute values of the measured mobilities.

LT form. Platelet crystals were laminated on pre-patterned electrodes on the Si/SiO_2 substrate (bottom-gate, bottom-contact). The devices operated as p-type (Fig. 7(b) and (c)), with a mobility of approximately 0.14 $cm^2\ V^{-1}\ s^{-1}$. This value is about one order of magnitude higher than that reported for single-crystal transistors of TBPy-C1,[34] which can be attributed to the more extended π-conjugated framework of the present molecule. As shown in the output and transfer characteristics

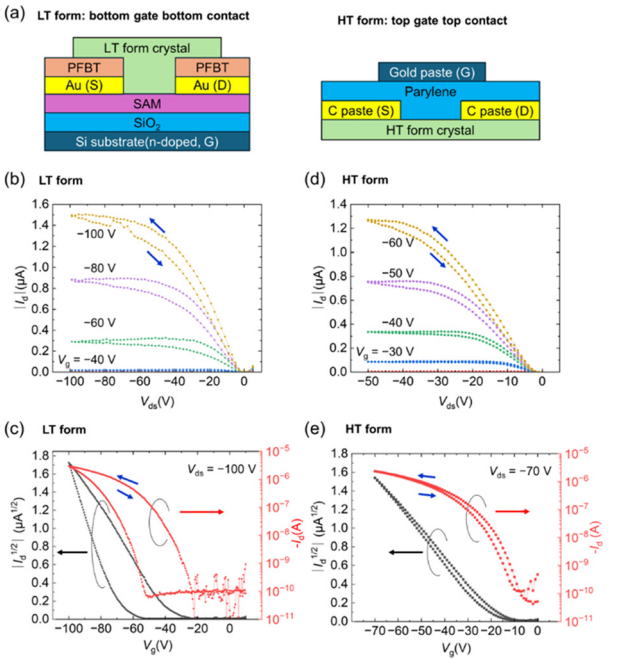

Fig. 7 (a) Schematic illustrations of the single-crystal transistor configurations for the LT (bottom-gate/bottom-contact) and HT (top-gate/top-contact) forms. (b and c) Output and transfer characteristics of the LT-form device. (d and e) Output and transfer characteristics of the HT-form device. structure. For the LT-form device: channel width W = 114 μm, channel length L = 57 μm, and gate capacitance per unit area C_i = 6.01 nF cm^{-2}. For the HT-form device: W = 93 μm, L = 187 μm, and C_i = 3.28 nF cm^{-2}. Mobilities were extracted from the saturation regime.

Open Access Article. Published on 28 January 2026. Downloaded on 5/23/2026 3:30:11 PM.
This article is licensed under a Creative Commons Attribution-NonCommercial 3.0 Unported Licence.

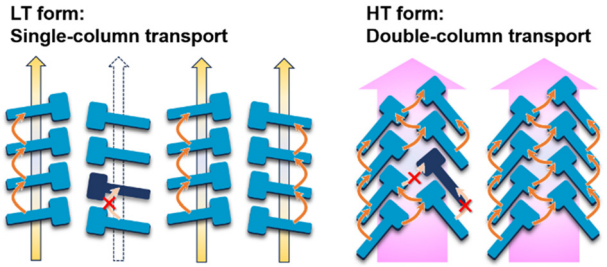

Fig. 8 Schematic diagram of the single-column transport and double-column transport.

(Fig. 7(c)), the drain current exhibited noticeable hysteresis, which is likely related to a higher density of trap states at the semiconductor–dielectric interface and/or within the crystal. The lower mobility compared with the theoretical value is also attributed to contact resistance and trapping effects.

HT form. Rod crystals were processed into top-gate, top-contact devices using parylene as the dielectric layer. The device also operates as p-type and the mobility of $\sim$1.2 $cm^2 V^{-1} s^{-1}$, about one order of magnitude higher than that of the LT form, in line with theoretical predictions (Fig. 7(d) and (e)). The superior performance stems from the pitched π-stacking and double-column transport, which enhance robustness against structural defects (Fig. 8). In addition, the drain current hysteresis was much smaller than that observed in the LT form, and the field-effect mobility showed weaker dependence on gate voltage (Fig. S7), suggesting a lower density of trap states and more stable carrier transport in the HT crystal. Although the use of different device configurations may affect the absolute mobility values, the experimentally observed trend—significantly higher mobility for the HT form than for the LT form—is consistent with the results of transfer-integral calculations, which are independent of device architecture. This agreement indicates that the enhanced charge-transport performance of the HT form primarily originates from its crystal packing and electronic coupling topology rather than from device-related factors.

Nevertheless, the experimental mobilities remained lower than the calculated values. Besides contact resistance and trapping effects, molecular deformation is expected to reduce orbital alignment, as deviations from the mirror plane weaken intermolecular overlap (Fig. S8). Temperature-dependent FET measurements showed no signs of a phase transition down to 150 K. Mobility decreased upon cooling, showing thermally activated behavior consistent with a hopping mechanism (see Fig. S9).[27,31] While the small λ_h and the large transfer integrals in the HT form would in principle support band-like transport, molecular deformation likely suppresses coherence. Pressure-dependent experiments are proposed as the next step, to shorten intermolecular distances, suppress deformation, and possibly induce band-like conduction.

Conclusions

In conclusion, two polymorphs of a new T-shaped π-conjugated molecule were obtained by PVT. The LT form adopts a θ-type packing motif that supports conventional one-dimensional charge transport, whereas the HT form crystallizes in a pitched π-stacking motif similar to rubrene. Despite its looser packing, the HT form exhibits shorter π–π distances and favorable orbital phase alignment, enabling strong coupling between two parallel π-stacking columns.

We define this cooperative pathway as ''double-column transport'', which represents a cooperative yet still one-dimensional transport topology and offers greater tolerance to defects compared with conventional single-column transport. Transfer integral calculations and single-crystal transistor measurements consistently show that the HT form achieves mobilities approximately one order of magnitude higher than the LT form. Importantly, the results reveal that charge-transport performance is governed not by packing density or the number of intermolecular contacts, but by orbital phase matching in these polymorphic organic semiconductors. The double-column transport architecture identified here provides a refined structural design principle for organic semiconductors. Suppressing molecular deformation—through external pressure or rational chemical design—may further improve orbital alignment and reduce dynamic disorder, potentially enabling a crossover from hopping-dominated to more coherent transport regimes. More broadly, deliberate control of cooperative columnar arrangements offers a promising route to robust, high-mobility materials for next-generation organic electronic devices.

Author contributions

S. J. performed synthesis, theoretical calculation and characterizations of the compounds. S. Y. contributed to the fabrication/evaluation of SC-FETs. All the X-ray crystallographic analyses were performed by P. J. and M. J. S. Y. and T. S. designed the present research project. The draft manuscript was written by S. J., S. Y., H. W. and T. S., and all the authors finalized the manuscript through proofreading. All authors approved the final version of the manuscript.

Conflicts of interest

There are no conflicts to declare.

Data availability

All data supporting the findings of this study are available within the article and its Supplementary information (SI). Supplementary information: powder X-ray diffraction (PXRD) patterns for both polymorphs, detailed crystallographic data, Hirshfeld surface analyses and corresponding fingerprint plots of intermolecular interactions, diffuse reflectance spectra, and molecular orbital overlap diagrams for both the HT and LT forms. Additional data provided in the SI comprise LUMO–LUMO transfer integrals, photographs of each transistor configuration, schematic illustrations showing the change in

This journal is © The Royal Society of Chemistry 2026

Open Access Article. Published on 28 January 2026. Downloaded on 5/23/2026 3:30:11 PM. This article is licensed under a Creative Commons Attribution-NonCommercial 3.0 Unported Licence.

orbital overlap induced by molecular deformation in the HT form, temperature-dependent transistor characteristics of the HT phase, and the gate-voltage dependence of the field-effect mobility for both polymorphs.

CCDC 2501061 and 2501062 contain the supplementary crystallographic data for this paper.[47a,b]

Acknowledgements

This work was supported by a JSPS KAKENHI Grant (No. 23K13714) and a grant from the Murata Science and Education Foundation. The computation was performed using the Research Center for Computational Science, Okazaki, Japan (Project: 25-IMS-C358) and the Supercomputer Center, the Institute for Solid State Physics, The University of Tokyo (2024-Ba-0054, 2025-A0010).

Notes and references

1 M. Sawatzki-Park, S. J. Wang, H. Kleemann and K. Leo, *Chem. Rev.*, 2023, **123**, 8232–8250.
2 G. Schweicher, G. Garbay, R. Jouclas, F. Vibert, F. Devaux and Y. H. Geerts, *Adv. Mater.*, 2020, **32**, 1905909.
3 Z. He, K. Asare-Yeboah and S. Bi, *Coatings*, 2024, **14**, 1080.
4 A. N. Sokolov, S. Atahan-Evrenk, R. Mondal, H. B. Akkerman, R. S. Sánchez-Carrera, S. Granados-Focil, J. Schrier, S. C. B. Mannsfeld, A. P. Zoombelt, Z. Bao and A. Aspuru-Guzik, *Nat. Commun.*, 2011, **2**, 437.
5 Y. Diao, K. M. Lenn, W. Y. Lee, M. A. Blood-Forsythe, J. Xu, Y. Mao, Y. Kim, J. A. Reinspach, S. Park, A. Aspuru-Guzik, G. Xue, P. Clancy, Z. Bao and S. C. B. Mannsfeld, *J. Am. Chem. Soc.*, 2014, **136**, 17046–17057.
6 J. Guo, C. Shi, Y. Zhen and W. Hu, *Acc. Mater. Res.*, 2024, **5**, 907–919.
7 V. Podzorov, E. Menard, A. Borissov, V. Kiryukhin, J. A. Rogers and M. E. Gershenson, *Phys. Rev. Lett.*, 2004, **93**, 086602.
8 C. Sutton, M. S. Marshall, C. D. Sherrill, C. Risko and J. L. Brédas, *J. Am. Chem. Soc.*, 2015, **137**, 8775–8782.
9 M. Moret and A. Gavezzotti, *New J. Chem.*, 2022, **46**, 7626–7637.
10 H. Moon, R. Zeis, E. J. Borkent, C. Besnard, A. J. Lovinger, T. Siegrist, C. Kloc and Z. Bao, *J. Am. Chem. Soc.*, 2004, **126**, 15322–15323.
11 H. Chung and Y. Diao, *J. Mater. Chem. C*, 2016, **4**, 3915.
12 C. C. Mattheus, G. A. De Wijs, R. A. De Groot and T. T. M. Palstra, *J. Am. Chem. Soc.*, 2003, **125**, 6323–6330.
13 T. Matsukawa, M. Yoshimura, M. Uchiyama, M. Yamagishi, A. Nakao, Y. Takahashi, J. Takeya, Y. Kitaoka, Y. Mori and T. Sasaki, *Jpn. J. Appl. Phys.*, 2010, **49**, 085502.
14 G. Giri, E. Verploegen, S. C. B. Mannsfeld, S. Atahan-Evrenk, D. H. Kim, S. Y. Lee, H. A. Becerril, A. Aspuru-Guzik, M. F. Toney and Z. Bao, *Nature*, 2011, **480**, 504–508.
15 S. Hutsch and F. Ortmann, *npj Comput. Mater.*, 2024, **10**, 206.
16 K. A. McGarry, W. Xie, C. Sutton, C. Risko, Y. Wu, V. G. Young, J. L. Brédas, C. D. Frisbie and C. J. Douglas, *Chem. Mater.*, 2013, **25**, 2254–2263.
17 P. He, Z. Tu, G. Zhao, Y. Zhen, H. Geng, Y. Yi, Z. Wang, H. Zhang, C. Xu, J. Liu, X. Lu, X. Fu, Q. Zhao, X. Zhang, D. Ji, L. Jiang, H. Dong and W. Hu, *Adv. Mater.*, 2015, **27**, 825–830.
18 Z. Zhang, L. Jiang, C. Cheng, Y. Zhen, G. Zhao, H. Geng, Y. Yi, L. Li, H. Dong, Z. Shuai and W. Hu, *Angew. Chem., Int. Ed.*, 2016, **55**, 5206–5209.
19 X. Ye, Y. Liu, Q. Han, C. Ge, S. Cui, L. Zhang, X. Zheng, G. Liu, J. Liu, D. Liu and X. Tao, *Chem. Mater.*, 2018, **30**, 412–420.
20 T. He, M. Stolte, C. Burschka, N. H. Hansen, T. Musiol, D. Kälblein, J. Pflaum, X. Tao, J. Brill and F. Würthner, *Nat. Commun.*, 2015, **6**, 5954.
21 Q. Guo, X. Ye, Q. Lin, Q. Han, C. Ge, X. Zheng, L. Zhang, S. Cui, Y. Wu, C. Li, Y. Liu and X. Tao, *Chem. Mater.*, 2020, **32**, 7618–7629.
22 J. E. Anthony, J. S. Brooks, D. L. Eaton and S. R. Parkin, *J. Am. Chem. Soc.*, 2001, **123**, 9482–9483.
23 Y. Sakamoto, T. Suzuki, M. Kobayashi, Y. Gao, Y. Fukai, Y. Inoue, F. Sato and S. Tokito, *J. Am. Chem. Soc.*, 2004, **126**, 8138–8140.
24 C. Wang, D. Hashizume, M. Nakano, T. Ogaki, H. Takenaka, K. Kawabata and K. Takimiya, *Chem. Sci.*, 2020, **11**, 1573–1580.
25 T. Yamamoto and K. Takimiya, *J. Am. Chem. Soc.*, 2007, **129**, 2224–2225.
26 T. Yamamoto, S. Shinamura, E. Miyazaki and K. Takimiya, *Bull. Chem. Soc. Jpn.*, 2010, **83**, 120–130.
27 M. J. Kang, I. Doi, H. Mori, E. Miyazaki, K. Takimiya, M. Ikeda and H. Kuwabara, *Adv. Mater.*, 2011, **23**, 1222–1225.
28 J. Mei, Y. Diao, A. L. Appleton, L. Fang and Z. Bao, *J. Am. Chem. Soc.*, 2013, **135**, 6724–6746.
29 S. Fratini, M. Nikolka, A. Salleo, G. Schweicher and H. Sirringhaus, *Nat. Mater.*, 2020, **19**, 491–502.
30 Z. Shuai, H. Geng, W. Xu, Y. Liao and J. M. André, *Chem. Soc. Rev.*, 2014, **43**, 2662–2679.
31 H. Meng, F. Sun, M. B. Goldfinger, F. Gao, D. J. Londono, W. J. Marshal, G. S. Blackman, K. D. Dobbs and D. E. Keys, *J. Am. Chem. Soc.*, 2006, **128**, 9304–9305.
32 S. Giannini and J. Blumberger, *Acc. Chem. Res.*, 2022, **55**, 819–830.
33 H. Oberhofer, K. Reuter and J. Blumberger, *Chem. Rev.*, 2017, **117**, 10319–10357.
34 R. Rubert-Albiol, D. Aranda, E. Ortí, J. Cerdá and J. Aragó, *J. Chem. Phys.*, 2025, **162**, 064105.
35 L. Zhang, Y. Zhao, J. Li, Y. Fu, B. Peng, J. Yang, X. Lu and Q. Miao, *J. Am. Chem. Soc.*, 2025, **147**, 3459–3467.
36 S. Kojima, T. Okamoto, K. Miwa, H. Sato, J. Takeya and Y. Matsuo, *Org. Electron.*, 2013, **14**, 437–444.
37 O. V. Dolomanov, L. J. Bourhis, R. J. Gildea, J. A. K. Howard and H. Puschmann, *J. Appl. Crystallogr.*, 2009, **42**, 339–341.
38 G. M. Sheldrick, *Acta Crystallogr., Sect. A: Found. Adv.*, 2015, **71**, 3–8.
39 C. F. Macrae, I. Sovago, S. J. Cottrell, P. T. A. Galek, P. McCabe, E. Pidcock, M. Platings, G. P. Shields, J. S. Stevens,

Open Access Article. Published on 28 January 2026. Downloaded on 5/23/2026 3:30:11 PM.
This article is licensed under a Creative Commons Attribution-NonCommercial 3.0 Unported Licence.

M. Towler and P. A. Wood, *J. Appl. Crystallogr.*, 2020, **53**, 226–235.

40 M. J. Frisch, G. W. Trucks, H. B. Schlegel, G. E. Scuseria, M. A. Robb, J. R. Cheeseman, G. Scalmani, V. Barone, G. A. Petersson, H. Nakatsuji, X. Li, M. Caricato, A. V. Marenich, J. Bloino, B. G. Janesko, R. Gomperts, B. Mennucci, H. P. Hratchian, J. V. Ortiz, A. F. Izmaylov, J. L. Sonnenberg, D. Williams-Young, F. Ding, F. Lipparini, F. Egidi, J. Goings, B. Peng, A. Petrone, T. Henderson, D. Ranasinghe, V. G. Zakrzewski, J. Gao, N. Rega, G. Zheng, W. Liang, M. Hada, M. Ehara, K. Toyota, R. Fukuda, J. Hasegawa, M. Ishida, T. Nakajima, Y. Honda, O. Kitao, H. Nakai, T. Vreven, K. Throssell, J. A. Montgomery Jr., J. E. Peralta, F. Ogliaro, M. J. Bearpark, J. J. Heyd, E. N. Brothers, K. N. Kudin, V. N. Staroverov, T. A. Keith, R. Kobayashi, J. Normand, K. Raghavachari, A. P. Rendell, J. C. Burant, S. S. Iyengar, J. Tomasi, M. Cossi, J. M. Millam, M. Klene, C. Adamo, R. Cammi, J. W. Ochterski, R. L. Martin, K. Morokuma, O. Farkas, J. B. Foresman and D. J. Fox, *Gaussian 16, Revision C.01*, Gaussian, Inc., Wallingford CT, 2016.

41 H. Kobayashi, N. Kobayashi, S. Hosoi, N. Koshitani, D. Murakami, R. Shirasawa, Y. Kudo, D. Hobara, Y. Tokita and M. Itabashi, *J. Chem. Phys.*, 2013, **139**, 014707.

42 Y. Mei, D. Fogel, J. Chen, J. W. Ward, M. M. Payne, J. E. Anthony and O. D. Jurchescu, *Org. Electron.*, 2017, **50**, 100–105.

43 P. R. Spackman, M. J. Turner, J. J. McKinnon, S. K. Wolff, D. J. Grimwood, D. Jayatilaka and M. A. Spackman, *J. Appl. Crystallogr.*, 2021, **54**, 1006–1011.

44 D. A. Da Silva Filho, E. G. Kim and J. L. Brédas, *Adv. Mater.*, 2005, **17**, 1072–1076.

45 T. Otaki, T. Terashige, J. Tsurumi, T. Miyamoto, N. Kida, S. Watanabe, T. Okamoto, J. Takeya and H. Okamoto, *Phys. Rev. B*, 2020, **102**, 245201.

46 C. Wang, H. Dong, W. Hu, Y. Liu and D. Zhu, *Chem. Rev.*, 2012, **112**, 2208.

47 (*a*) CCDC 2501061: Experimental Crystal Structure Determination, 2026, DOI: 10.5517/ccdc.csd.cc2pykdm; (*b*) CCDC 2501062: Experimental Crystal Structure Determination, 2026, DOI: 10.5517/ccdc.csd.cc2pykfn.

 This journal is © The Royal Society of Chemistry 2026